

Coronal Plasma Diagnostics from ground based observations

E. Landi¹, S.R. Habbal², S. Tomczyk³

Author Manuscript

¹Department of Climate and Space Sciences and Engineering, University of Michigan, Ann Arbor, MI, USA

²Department of Astronomy, University of Hawaii, Honolulu, HI, USA

³High Altitude Observatory, Boulder, CO, USA

This is the author manuscript accepted for publication and has undergone full peer review but has not been through the copyediting, typesetting, pagination and proofreading process, which may lead to differences between this version and the Version of Record. Please cite this article as doi:10.1002/2016JA022598

D R A F T August 31, 2016, 2:18am

D R A F T

Key Points.

- We compare the characteristics of coronal observations in the visible with those carried out in the EUV and X-ray wavelength ranges.
- We review the diagnostic techniques to measure coronal plasma parameters, and magnetic field with coronal spectral lines in the visible wavelength range.
- We describe the future ground-based coronagraphic instrumentation to observe the solar corona in the visible wavelength range.

Abstract. In this paper we discuss the potential of ground-based visible observations of the solar corona to address the key open problems in the physics of the solar atmosphere and of solar activity. We first compare the diagnostic potential of visible observations with those of high-resolution spectrometers and narrow-band imagers working in the EUV and X-ray wavelength ranges. We then review the main diagnostic techniques (and introduce a few new ones) that can be applied to line and continuum emission in the solar atmosphere, and the physical problems that they enable us to address. Finally, we briefly review the main features of ground-based coronagraphic instrumentation currently being developed and planned.

Author Manuscript

1. Introduction

The solar corona has critical importance for the solar-terrestrial relationship, as it hosts a number of phenomena that directly affect the Earth. For example, flares and Coronal Mass Ejections (CMEs), the most important Space Weather events, are initiated in the corona: flare radiation influences the density of the upper atmosphere and can perturb satellite trajectories and performances; CMEs can disrupt communications, power grids and pose health hazards to astronauts and even to airplane passengers traveling on polar routes. However, the processes that store and release the plasma and energy involved in these events are still poorly understood. This, however, is not the only limitation in our understanding of the solar atmosphere. In fact, the solar corona is heated to multimillion degree temperatures, but the mechanisms that provide the required energy to maintain those temperatures are unknown; the solar wind, accelerated from the solar atmosphere, shapes the heliosphere and its characteristics, but still its origin is not understood; the composition of the solar corona is subject to fractionation processes that differentiate it from that of the underlying photosphere, which have not yet been identified. Also, solar activity is strongly dependent on the 22-year solar magnetic cycle, which we are still unable to predict.

Even if we still do not understand some of the fundamental properties of the solar atmosphere, one thing is clear: all these phenomena are related to the magnetic field that pervades the solar atmosphere and organizes the plasma in structures at all scales. Several theories have been proposed on how magnetic energy is released into solar plasmas and how it accelerates them, but progress in discriminating among them has been hindered

by one fundamental fact: we do not have measurements of the magnetic field in the solar corona. This lack of data is due to the intrinsic difficulty of measuring the magnetic field. The magnetic field produces the Zeeman and the Hanle effects on solar radiation; the Zeeman effect scales as λ^2 , where λ is the wavelength, so that its signatures are far easier to observe in the visible than in the EUV and X-ray wavelength ranges. Hence, the fleet of space-borne EUV and X-ray instruments currently at our disposal are of little help. The Hanle effect has been observed in a few far UV coronal lines using slit spectrometers, but their field of view is too limited. However, both processes can be detected in the visible spectral range, through polarimetry and high resolution spectroscopy of coronal spectral lines.

The observations which ideally will provide the tools to solve the problems of coronal heating, wind acceleration, and solar activity, need to fulfill the following requirements:

1. provide measurements of the magnetic field;
2. provide simultaneous 2D images of the solar corona;
3. provide spectroscopic diagnostic tools to measure the plasma parameters simultaneously in the entire corona;
4. allow the measurement of plasma dynamics;
5. allow monitoring of the entire corona at good cadence over long time periods.

Here we describe how a ground based coronagraph can provide observations that fulfill all these requirements, and which methodologies need to be used to measure the magnetic field and plasma properties of the solar corona. We first compare the main features of space-borne X-ray and EUV instrumentation with ground-based visible observatories (Section 2), then we describe the diagnostic techniques that can be used to measure the

magnetic, thermodynamic and dynamic properties of the solar atmosphere (Section 3) and the science questions that they can address (Section 4). Section 5 provides a brief overview on coronagraphic instrumentation of the future.

2. Advantages of a ground-based coronagraph for the solar corona

The invention of the coronagraph by B. Lyot (1932) made daily ground-based observations of the solar corona in the visible wavelength range a reality. This instrument paved the way for coronagraphic observations of the solar atmosphere in broad-band white light and narrow-band spectral lines, coupled with polarimetry to infer the direction and strength of the magnetic field (e.g. Arnaud & Newkirk 1987, Lin et al. 2004, Tomczyk et al. 2007).

Space-based observatories, on the other hand, starting with the launch of Skylab in 1973, paved the way for exploiting the diagnostic capabilities of the UV, EUV and X-ray emission. However, because of the strong dependence of the emission in these wavelength ranges on coronal density, the diagnostic potential of UV, EUV and X-ray spectroscopy and imaging is still limited to a small height above the photosphere (below $1.5 R_{sun}$ in heliocentric coordinates). Also, no magnetic field diagnostics exists for X-ray and EUV radiation.

The only exceptions are PROBA2/SWAP and SoHO/UVCS. The former can obtain images of the large scale corona up to ≈ 2 solar radii in one EUV narrow band centered at 174 \AA . However, it has limited diagnostic capabilities, because it only has one channel, and cannot resolve spectral line profiles. SOHO/UVCS encompassed the $1.5-10 R_{sun}$ height range, but its spatial and temporal resolution were very low, due to the long integration times (hours) and the need to rebin the image to reach a reliable signal to noise ratio.

Visible observations of multiple coronal line intensities have many qualities that make them unique:

1. They can provide measurements of the magnetic field;
2. By observing individual spectral lines, they retain the same high temperature discriminating potential as high-resolution EUV spectrometers, and multiple lines can provide measurements of the thermal structure of large-scale plasma coronal structures;
3. Through the use of tunable filtergraphs, they can measure line profiles with high spectral resolution almost simultaneously over the entire off-disk corona at high spatial resolution;
4. They can extend the limited field of view of UV, EUV and X-ray emission out to several solar radii, in the critical region for solar wind and CME acceleration;
5. Combining Doppler shifts and observations of motions in the plane of the sky through series of 2D images, they can measure the velocity vector;
6. Using spectral line widths, they can determine unresolved motions.

In other words, instruments observing in the visible range can combine in one single optical design the advantages of *both* EUV narrow band imagers and EUV high resolution spectrometers, extending their field of view up to several solar radii.

For example, Figure 1 shows the image of the solar corona taken with the SDO/AIA 171 Å channel on 11 July 2010 during a total solar eclipse, together with a white light image of the whole corona taken simultaneously from the ground. The larger field of view of the white light image allows the identification of several large scale structures beyond the EUV imager's field of view. While Figure 1 shows white light integrated emission, similar images can be obtained using coronal emission lines in the visible range, where

the full line profile is measured at every pixel nearly simultaneously, vastly improving the temperature and diagnostic purity of the image.

Also, easy access to a ground instrument allows hardware repair and upgrade. It thus ensures longer operational lives compared to space instruments, and the acquisition of self-consistent observations of the solar corona over long periods of time. Such advantages minimize the problems produced by inter calibration and observational consistency which affect measurements from different space instruments. Furthermore, any technical problem in space-based instrumentation can irreversibly decrease its capability. For example, detector degradation severely limited SOHO/SUMER observations early in the SoHO mission to a few campaigns each year; the Hinode high gain antenna failure which occurred in 2008 severely limit the data volume that can be downloaded from the instrument. Hence, despite the main disadvantages of the visible ground-based observations, namely (1) the corona can only be observed outside the solar disk, and (2) the observations are prone to weather increment, these measurements still offer superior diagnostic potentials, when compared to space-based instruments, as will be described next.

However, there are two main disadvantages. First, the solar corona can only be observed outside the disk. Second, ground based observatories can observe the Sun only during the day, and their observations are prone to interruptions due to the weather. On the other hand, any technical problem in space instrumentation can decrease the observations of space instruments to well below the capabilities of a ground based instrument. For example, detector degradation severely limited SOHO/SUMER observations early in the SoHO mission to a few campaigns each year; the Hinode high gain antenna failure

which occurred in 2008 severely limited the data volume that can be downloaded from the instrument.

3. Visible plasma diagnostic techniques

3.1. Formation mechanisms of visible coronal emission

The intensity I_{line} of a spectral line emitted by a transition from level j to level i of charge state q for element X is given by

$$I_{line} = I_{coll} + I_{rad} \quad (1)$$

$$I_{coll} = \frac{1}{4\pi} \int_0^\infty G(T, n_e) \varphi(T) dT \quad (2)$$

$$I_{rad} = \frac{B A_{ji}}{4\pi A_{tot}} \int_{-\infty}^\infty N_{abs} p(\phi) F_{inc} D(v) dx \quad (3)$$

where I_{coll} and I_{rad} are the collisionally and radiatively excited components, respectively. T is the electron temperature, dT and dx lie along the line-of-sight (taken to be the x axis), F_{inc} is the intensity of the incident radiation, $p(\phi)$ is the scattering factor and $D(v)$ is the Doppler Dimming term (see Phillips et al. 2008 for a definition), B is the Einstein absorption coefficient, A_{ij} is the Einstein coefficient for spontaneous emission of the transition, while A_{tot} is the total decay rate from the upper level via spontaneous emission. The Differential Emission Measure (DEM) $\varphi(T)$ of the plasma, the line Contribution Function $G_{ji}(T, n_e)$ and the number of absorbers N_{abs} are defined as

$$G_{ji}(T, n_e) = \frac{n_j(X^{+q})}{n(X^{+q})} \frac{n(X^{+q})}{n(X)} \frac{n(X)}{n(H)} \frac{n(H)}{n_e} \frac{A_{ji}}{n_e} \quad (4)$$

$$\varphi(T) = n_e^2 \frac{dx}{dT} \quad (5)$$

$$N_{abs} = \frac{n(X^{+q})}{n(X)} \frac{n(X)}{n(H)} \frac{n(H)}{n_e} n_e \quad (6)$$

where $n_j(X^{+q})/n(X^{+q})$ is the relative population of the upper level j for charge state X^{+q} , $n(X^{+q})/n(X)$ is the relative abundance for charge state q of element X , $n(X)/n(H)$ is the abundance of X relative to hydrogen, and $n(H)/n_e$ is the hydrogen density relative to that of free electrons. Close to the Sun, $I_{rad} \ll I_{coll}$ for the majority of EUV spectral lines, but its contribution to lines emitted in the visible is significant or even dominant at a distance as low as $1.1 R_{sun}$ (e.g. Habbal et al. 2011). The dependences of I_{coll} and I_{rad} on the electron density are different: through the DEM, the collisional component depends on n_e^2 , while the radiative component depends on n_e .

The intensity I_{cont} of the solar continuum radiation is due to Thomson scattering of photospheric radiation by coronal free electrons; it is also dependent on n_e and can be written as:

$$I_{cont} = \int dx n_e(x) \int d\Omega Q(\Omega) \int d\lambda f(\lambda) I_{sun}(\lambda, \Omega) \quad (7)$$

where $I_{sun}(\lambda, \Omega)$ is the incident radiation from the solar photosphere at wavelength λ coming from the direction Ω , $Q(\Omega)$ is a geometrical factor which also includes the Thomson scattering cross section, and $f(\lambda)$ takes into account the velocity distribution of the scattering free coronal electrons (see Cram 1976 for details).

The solar disk radiation scattered by Earth's atmosphere is far brighter than the corona itself. While coronal spectral lines can be easily retrieved by subtracting the sky emission in the continuum adjacent to the spectral line, such a method is not applicable to the coronal continuum itself. This problem can be in part overcome considering that the Thomson scattering in the corona occurs at nearly 90 degrees angle between the line of sight and the direction of the exciting radiation, so that the emission is polarized, while the

atmospheric scattering of solar radiation close to the disk occurs along the perpendicular direction and hence does not introduce any additional polarization. Thus, the polarized component of the solar corona can be retrieved through the use of polarimeters.

As the electron density decreases with height, I_{coll} decreases much faster than I_{rad} and I_{cont} . This different dependence explains why the emission from visible lines, which has a very strong component I_{rad} , can be observed well beyond $2 R_{sun}$, while the emission from EUV lines, whose I_{rad} is much lower, can be observed beyond $1.5 R_{sun}$ only with great difficulty.

3.2. Magnetic field measurements

Coronagraphic observations in broad-band white light and narrow-band spectral lines, coupled with polarimetry to infer the direction and strength of the magnetic field have been proposed in the past (Arnaud & Newkirk 1987). Judge et al. (2001) carried out a thorough assessment of various methods to measure the magnetic field of the solar corona, and concluded that the most promising techniques involved polarimetry of spectral lines. In particular, they recommended longitudinal Zeeman effect, measured through circularly polarized radiation, to measure the magnetic field component along the line of sight, and resonance polarization, resulting in linearly polarized lines, to determine the magnetic field orientation in the plane of the sky. Such measurements are easiest when using M1 lines emitted in the visible by coronal ions.

These measurements are not without limitations. Judge et al. (2013) reviewed the polarimetric measurements from these types of lines by studying the mechanisms that generate polarization in the lines themselves. The ratio between the U and Q stokes parameters is proportional to the magnetic azimuth in the plane of the sky, but the large

radiative lifetime of M1 lines causes this ratio to be independent of the magnetic field magnitude B , so that we are left with only the magnetic azimuth. On the contrary, the measurement of Stokes parameter V is proportional to the product $B \cos \Theta_B$, where Θ_B is the inclination of the magnetic field vector with the line of sight. However, the magnitude of V is proportional to the first derivative of the spectral line profile, making this measurement difficult due to the small value of this quantity. Still, these are the best measurements we can make of the coronal magnetic field.

Even with these limitations, visible polarization measurements can provide critical info on magnetic structures on the Sun. For example, Rachmeler et al. (2013) concluded that coronal polarization measurements could unambiguously discriminate between different polar crown-filament magnetic configurations (cylinder, flux rope, spheromak, sheared arcades) providing critical information on the structure, stability, and possible eruption of these structures. Bak-Steslika et al. (2013) found from CoMP magnetic field measurements that prominence cavities are consistent with a magnetic flux rope model.

3.3. Continuum polarized brightness and the electron density

In principle, the Thomson-scattered continuum radiation can be used for a variety of diagnostic purposes. However, as discussed in Section 3.1, the presence of atmospheric scattering of disk radiation in observations from the ground greatly complicates the observations of the coronal continuum. Outside eclipses, only the polarized component of the coronal continuum can be recovered from observations.

Van de Hulst (1950) developed a technique to retrieve the coronal free electron density from the polarized brightness of the coronal continuum. This technique also exploited the fact that the F-corona in the vicinity of the solar disk is also unpolarized and can

be subtracted together with the radiation scattered by the atmosphere. The polarized brightness pB of the corona at a point x in the off-disk corona can be expressed as (Hayes et al. 2001):

$$pB(x) = C \int_x^\infty N(r)[A(r) - B(r)] \frac{x^2}{r\sqrt{r^2 - x^2}} dr \quad (8)$$

where C is a constant, $N(r)$ is the electron density, $A(r)$ and $B(r)$ are geometrical factors provided by van de Hulst (1950), x is the projected heliocentric distance of the point, and r is the radial height from Sun center. The electron density $N(r)$ is retrieved after expanding it in polynomial form and inverting Equation 8 to determine the coefficients. This technique has been universally used for coronal density measurements from ground and space instruments, and it has been extended to the total continuum brightness B by Hayes et al. (2001).

A large body of measurements of coronal density from visible pB and B observations have been obtained from ground based observatories such as Mauna Loa Solar Observatory (MLSO) and SoHO/LASCO. Frazin et al. (2010) carried out a comparison between the two instruments, and utilized such measurements for 3D reconstruction of the density structure of the solar corona.

3.4. Line-to-line intensity ratios

A line-to-line intensity ratio in the visible wavelength range has three regimes, found at increasingly larger heights: 1) both lines are collisionally excited; 2) one or both lines are transitioning from collisional to radiative excitation; 3) both lines are radiatively excited.

When spectral line formation is dominated by collisional excitation, the standard plasma diagnostics applied to EUV lines (described in Phillips et al. 2008) can be used for the analysis of visible coronal lines. These techniques allow us to measure the plasma DEM $\varphi(T)$, the plasma electron density and elemental composition. It is important to note that photoexcitation can be an important factor in the level population balance even before radiative scattering dominates spectral lines, and its importance depends on the local plasma density so that it can not be accounted for a priori. Photoexcitation affects both coronal visible lines and EUV lines, as it alters the level population of metastable levels and hence of the entire ion. The line intensity ratios most commonly used for density diagnostics are Fe XIII 10800/10747, Ni XV 6703/8026, Ca XV 5446/5696, and Ar XIII 8339/10145. In the past, these ratios have been extensively used to measure plasma electron density in the corona (e.g. Landi & Bhatia 2012 and references therein).

The intensity of a radiatively excited visible line depends primarily on the abundance $n(X^{+q})/n(X)$ of the ion from which it is emitted: when both lines a and b from two ions of the same element are radiatively excited, their ratio depends on the ratio of the abundances of the two ions, and can be used to determine this quantity. This is of critical importance, because charge state ratios are one of the main solar wind parameters measured by in-situ mass spectrometers, after they are frozen-in. Visible line intensity ratios can be used to monitor the evolution of the charge state ratios with distance from the Sun everywhere in the corona both in closed field structures and in the solar wind, to directly connect coronal observations and in-situ measurements. Despite its relative simplicity, this diagnostic technique has never been used in the past, and work is in progress to apply it to eclipse data.

3.5. Line-to-continuum intensity ratios

Even if a ground-based coronagraph is unable to retrieve the total continuum intensity, the polarized component alone can be used in combination with spectral line intensities to carry out plasma diagnostics.

The line-to-continuum intensity ratios can indicate the height at which the line intensity changes its excitation mechanism from collisional to radiative. In fact, when the collisional component dominates, this ratio is approximately proportional to n_e , when the line is formed by radiative scattering this ratio no longer depends on n_e and hence evolves much more slowly with distance. Thus, this ratio allows us to determine the height R_{rad} where the transition from the collisional to radiative regimes occurs. An example, taken during the 29 Mar 2006 eclipse, is shown in Figure 2 (Habbal et al. 2007). Using eclipse visible observations where the total continuum could be observed, Habbal et al. (2010a,b,c, 2011) showed that this height is much closer to the solar disk than anticipated, within the field of view of available remote sensing instrumentation.

Habbal and co-workers used eclipse data, where both polarized and unpolarized components of the continuum could be observed. However, such a measurement is possible also using the polarized component of the continuum that a ground coronagraph observes.

Such a ratio can in principle be used to determine the absolute value of the abundance of the ion emitting the spectral line; a critical parameter to study solar wind acceleration and connect in-situ and remote sensing observations. During eclipses and from space, this measurement can be done as the total continuum can be measured. However, from the ground it is necessary to determine the degree of continuum polarization, which is non trivial since this quantity is a complex function of distance from the photosphere

and it depends on the plasma structures in the corona (Skomorovski et al. 2012). Still, these measurements are possible during eclipses where the Earth's atmosphere scattering is absent.

3.6. Large scale temperature distribution of the extended corona

Habbal et al. (2011) showed that large scale structures in the solar corona were markedly different when observed with different coronal visible lines, even when these lines were formed at very similar temperatures, like Fe X and Fe XI (1.1×10^6 versus 1.35×10^6 K, Del Zanna et al. 2015). An example is shown in Figure 3, where the solar corona as observed with Fe X, Fe XI and Fe XIV is shown: different ions, highlighted by different colors, show different large-scale structures, demonstrating the temperature resolving power of their emission (from Habbal et al. 2011). This indicates that these structures are near-isothermal, so that visible observations of many lines formed over a wide range of temperatures can help us make a map of the thermal structure of the large scale corona. In general, when lines are collisionally excited, standard DEM techniques used for EUV and X-ray lines can be used to determine the plasma DEM. When radiative excitation dominates, Equations 3 and 6 allow us to apply inversion techniques to determine the $n_e(T)$ distribution along the line of sight.

Determinations of the thermal structure of the inner solar corona are routinely made with EUV and X-ray instrumentation, but these determinations are limited to the field of view of these instruments, which extends up to ≈ 1.5 solar radii. Beyond that height very few measurements have been made despite the importance of these outer regions for coronal heating studies, solar wind evolution and CME propagation. In the same way, the CME thermal structure has been seldom measured in the inner corona, and no

continuous monitoring of the evolution of the CME properties has been done because of the slow measurement cadence and the limited field of view. These measurements are possible using coronagraphic observations of spectral lines in the visible range.

3.7. Determination of vector velocities

When the spectral profiles of visible coronal lines is available, direct measurements of Doppler shifts can be done, providing information on the plasma velocities along the line of sight in all open and closed field structures. At the same time, time series of 2D images of the whole corona in the same lines provide a direct observation of dynamics in the plane of the sky. The combination of these two measurements allows us to reconstruct the velocity vector.

While these measurements may be difficult or ambiguous in closed field structures and in the solar wind, where individual plasma parcels are very difficult to identify and follow, they are of critical importance for CMEs, as they allow us to determine the velocity vector of the accelerating plasma at all times during the very initial phases of the eruption. This capability, together with the availability of lines formed in a wide temperature range, will allow us to measure the acceleration of all components of the CME plasmas, determine their kinetic energies, as well as whether nearby plasma structures deflect/change the CME trajectory at the very beginning of the acceleration. Tian et al. (2013) provided the first measurements of CME dynamics from visible spectral lines observed by COMP and discussed their diagnostic potential and limitations. In particular, they found that CMEs presented very large perturbations in the line centroid and large enhancements in their widths; these changes were even more pronounced than changes in the intensity of the Fe XIII line they were measured with, and in some cases they were located *ahead*

of the erupting prominence at the CME core. Also, Tian et al. (2013) showed that by combining measurements of the plasma Alfvén speed from loop oscillations excited by the CME event with density measurements obtained with the Fe XIII line pair observed by CoMP it was possible to retrieve the coronal magnetic field strength.

3.8. Determination of unresolved motions

Spectral line widths are formed by two distinct dynamical contributions: thermal motions, characterized by the ion temperature T_{ion} , and non-thermal motions. The Full Width Half Maximum $FWHM$ of an optically thin spectral line is given by

$$FWHM = \frac{\lambda_0}{c} \sqrt{4 \log 2 \left(\frac{2k_B T_i}{M} + v_{nth}^2 \right)} \quad (9)$$

where c is the speed of light, λ_0 is the rest wavelength, k_B is the Boltzmann constant, T_i is the ion temperature, M is the ion mass and v_{nth} is a non-thermal velocity parameter which describes the unresolved, non-thermal motions of the ion. Line width measurements can thus provide critical information on the location of shocks, of turbulence, of ion heating in both closed and open magnetic field structures, identify sub-resolution rotating structures, to name a few, as discussed by Tian et al. (2013).

3.9. Solar wind empirical modeling

The observations of multiple Fe lines, along with UV and EUV spectral lines observed from space, can be used to apply the solar wind diagnostic technique developed by Landi et al. (2012, henceforth L12). This technique utilizes user-defined velocity, electron temperature and electron density as a function of distance to calculate the evolution of the ion abundances in the wind plasma (using the Michigan Ionization Code – MIC, Landi

et al. 2012b). The ion abundances are then used to predict spectral line intensities and frozen-in charge states. These predictions can then be compared to observed line intensities and to in-situ measurements. Disagreements between predictions and measurements lead to corrections to the initial velocity, electron temperature and electron density profiles, which can be fed again into MIC. This procedure is repeated iteratively to improve the comparison results until agreement between predictions and observations is achieved. The final result is an empirical, data-driven model of the wind plasma velocity, electron temperature and electron density profiles, that can be compared to solar wind models.

The predictions of individual ion abundances as a function of distance allow the calculation of individual line intensities using Eqs. 3 and 6, because all plasma parameters are available from the MIC input and output physical parameters. Landi et al. (2014) applied this technique to spectral lines observed by SUMER below 1.3 solar radii, such as the Na IX line shown in Figure 4 (from Landi et al. 2014). The limited field of view was dictated by the rapid decrease of the collisionally dominated Na IX intensity. Visible observations, on the other hand, can extend this technique to much larger distances, in the critical region where solar wind heating and acceleration takes place, and solar wind charge states evolve and eventually freeze-in.

4. Science goals that can be addressed

Spectrally resolved observations of visible lines will allow us to address a multitude of different open questions in solar and heliospheric physics. Here we limit the discussion to a few of them.

4.1. Solar wind evolution in the solar corona

Knowledge of the charge state values and charge state ratio between two ions of the same element is very important. In fact, in open field regions of the solar corona, where the solar wind is expected to be flowing into the heliosphere, both quantities can provide two contributions to solar wind science of critical importance. First, they allow us to monitor the evolution of the charge state distribution in the inner corona for the first time, and when they become constant at a certain height, they provide a direct measurement of the freeze-in height and frozen in ratio value for the two ions; both quantities can be directly compared to in-situ measurements in the heliosphere, providing a direct, quantitative link between remote sensing observations and in-situ measurements of wind properties. Second, they provide empirical constraints to the wind plasma electron density, temperature and bulk speed using the technique outlined in Section 3.9. These provide critical quantitative constraints to theoretical models, and can also be used to validate models themselves, as shown by Landi et al. (2014).

4.2. Long term evolution of the extended corona

The physical properties and the structure of the solar corona evolve dramatically during the well known 11-year magnetic cycle of the Sun. During minima, the structure of the solar corona resembles that of a dipole, with coronal holes and open magnetic field structures at the poles, and a belt of closed field structures at the equator; during these periods CMEs occur once a day or less, and flares are infrequent and emit low levels of X-ray emission. During maxima, the solar atmosphere is a very complex mix of open and closed magnetic field structures, and hosts a large number of sunspots and active

regions which are the birthplace of numerous CMEs (several each day on average) and very energetic solar flares.

However, not all solar cycles are the same, and the most recent solar cycle 24 has surprised predictions by being the weakest in a century. The average number of sunspots, however, shows that the current solar cycle 24 is more in line with the average of the last 250 years, and that the cycles in the 20-th century have been unusually strong (McCraken et al. 2013). A strong solar cycle has deep effects on the heliosphere, because the larger radiation and particulate output in a strong cycle leads to significant changes in the properties of the interplanetary space. Also, the strength of the solar cycle, by strongly influencing the X-ray and EUV irradiance of the solar corona, can affect significantly the outermost layers of the Earth's atmosphere, changing its density and thus affecting artificial satellite orbits in the long term.

The causes of the modulation of the solar cycle, and of the presence of the solar cycle itself, and its effects on the solar corona and solar X-ray and EUV irradiance are not yet understood because of the lack of long term observations of the main physical properties of the solar atmosphere: its magnetic field, and its thermal and dynamic properties. Available observations have been taken by a host of different instruments working at different wavelength ranges and observing different regions of the solar atmosphere with different techniques: this raises a formidable obstacle for obtaining a multi-cycle consistent picture of the evolution of the solar corona. Ground-based instruments (easy to maintain and repair) can provide all the necessary measurements and diagnostics to study the solar corona and the solar wind, and will allow us to monitor the evolution of the solar

atmosphere through several solar cycles, providing a set of consistent observations and diagnostic measurements for decades.

4.3. Plasma diagnostics of erupting CMEs

Modeling CMEs and predicting their geoeffectiveness requires an accurate understanding of the energetics of these events. How much energy is released in those events, where it comes from, how is it distributed among different CME components, and in what fraction is it spent in heating and in accelerating the CME plasmas, are critical pieces of information for reliable CME modeling. However, current space instruments (broad band white light coronagraphs, EUV and X-ray narrow band imaging instruments, and EUV high resolution spectrometers) are unable to provide the required data: 2D series of images taken with many different spectral lines formed at all temperatures between $\approx 10,000$ K to several millions degrees, where the entire line profile is observed nearly simultaneously in each pixel.

The use of tunable filters, the large field of view, and the inclusion of a number of visible lines spanning the required temperature range, enable visible coronagraphs to provide the capabilities for near-simultaneous diagnostics of the thermal, magnetic and density structure of all CME components, and of the reconstruction of the dynamics continuously from CME onset to a few solar radii. These measurements encompass the region where a large fraction of the total energy of the CME event has already been released into CME plasma heating and acceleration. Tian et al. (2013) already showed that such studies are possible.

4.4. Coronal heating by magnetic waves

One of the leading proposed mechanisms for heating the solar corona (and accelerating the solar wind) is dissipation of magnetic waves. This method powers many first-principle, physics-based global coronal models, such as the Alfvén Wave Solar Model (van der Holst et al. 2014). There are many mechanisms proposed for how to dissipate magnetic waves and release their energy into the solar atmosphere, but all require observational evidence. For example, Hahn et al. (2012) showed that EUV spectral line widths in coronal holes increase with height consistently with the propagation of undamped magnetic waves, but at around $1.3 R_{sun}$ they suddenly start to decrease: interpreting such a decrease with wave damping, Hahn et al. (2012) determined that the rate of wave energy decrease was consistent with the heating requirements of coronal holes. However, such measurements are hampered by the small field of view and limited heights of EUV spectrometers.

Visible coronagraphs using tunable filters can resolve the profiles of many spectral lines in the solar corona to altitudes which are not reached by EUV spectrometers, and carry out long series of simultaneous measurements of line profiles across the entire corona (in contrast with the slit-like field of view of EUV spectrometers). These observations will allow us to develop maps of wave propagation and damping, as well as of wave frequency and propagation speed at multiple temperatures. Pioneering measurements of magnetic waves in the corona have already been carried out with CoMP (Tomczyk et al. 2007).

Some models of the solar corona based on Alfvén waves predict that towards the top of large scale loops the ion and electron temperatures decouple, as electrons are able to conduct the energy deposited by Alfvén waves downwards along the loop, while ions are much less efficient at that (van der Holst et al. 2014). This leads to a strong enhancement

of T_{ion} at the loop top while the electron temperatures is almost constant; this increase strongly affects line widths while keeping their intensities unchanged. This effect is predicted to occur at heights outside the reach of current EUV spectrometers but well within the ground coronagraphs field of view: it is a direct observable of wave-induced coronal heating, which can be directly studied using the spectrally resolved observations of coronal lines.

By detecting MHD wave phase speeds from time series of coronal images, these instruments will also provide the transverse magnetic field, allowing us to reconstruct the full magnetic field vector.

5. Future instrumentation

5.1. The UCoMP instrument

UCoMP will be an upgraded version of the existing Coronal Multichannel Polarimeter (CoMP) instrument (Tomczyk et al. 2008). CoMP comprises a 20-cm coronagraph followed by a polarimeter and a narrowband tunable birefringent filter that forms simultaneous images of the corona and continuum over a $2.8 R_{sun}$ field of view centered on the Sun at each selected wavelength. CoMP, currently operating at the Mauna Loa Solar Observatory, provides near-simultaneous 2D measurements of line width, intensity, Doppler velocity, and Stokes Q, U, V parameters of the entire corona in the 1.03 - $1.38 R_{sun}$ range using the 10747 \AA and 10798 \AA Fe XIII coronal lines, and the 10830 \AA He I chromospheric line with a spatial sampling of 4.6 arcsec per pixel and a spectral bandpass of 1.3 \AA .

The UCoMP upgrade, under development with NSF funding, will be described in detail in a separate publication and will only be described briefly here. The 20-cm *One Shot* coronagraph (Smartt, Dunn and Fisher, 1981) utilized by the CoMP instrument

will also be used by the UCoMP. Like CoMP, UCoMP will obtain images of the corona and continuum simultaneously in separate beams. The 1024 x 1024 camera in CoMP will be replaced by dual 1280 x 1024 cameras and the spatial sampling will be improved from 4.6 to 3 arcsec per pixel. The slow switching (250 ms switching time) CoMP polarization modulator based on Nematic liquid crystals will be replaced with a modulator employing Ferro-electric liquid crystals (<1 ms switching time) based on the polychromatic modulator implementation (Tomczyk et al. 2010). The calcite crystals in the CoMP birefringent filter will be replaced with Lithium Niobate crystals and the filter aperture will be increased from 35 mm to 50 mm to accommodate the larger field-of-view. The linear polarizers and half-waveplates in the birefringent filter will be replaced with wire grid polarizers and super achromatic waveplates, respectively. It is expected that the upgrade will be completed by July of 2017.

UCoMP will improve on the capabilities of the CoMP instrument in two significant ways. First, the wavelength range will be extended to include visible and near-IR emission lines in the 5000-11000 Å range. Second, the field-of-view of the UCoMP will be increased to 1.6-2.5 R_{sun} in heliocentric coordinates, as shown in Figure 5. This upgrade will allow UCoMP to observe a much larger number of coronal lines, as listed in Table 1. These lines are emitted by the quiescent and active corona in the 0.8-5.0 MK temperature range, as well as by the core of accelerating CMEs between 0.01 MK up to ≈ 0.5 MK. The additional ions observed by UCoMP will provide improved plasma diagnostic capabilities over the Fe XIII coronal lines provided by CoMP and will allow UCoMP to explore the feasibility of polarization measurements with other spectral lines, formed at different temperatures, in order to sample the solar coronal magnetic structure more thoroughly. The increased

field-of-view of UCoMP will be more than double that of the CoMP. It will allow improved tracking of CMEs, provide observations of coronal structures that are currently limited by the CoMP field-of-view and allow MHD wave observations out to much greater heights. By utilizing tunable filters to observe resolved emission lines, UCoMP will combine the strengths of simultaneous 2D imaging and high resolution spectroscopy into one single instrument.

5.2. The COSMO Observatory

COSMO consists of a suite of ground-based telescopes aimed at studying the solar corona. This suite of instruments is centered on the Large Coronagraph (LC), currently in advanced planning phase, which will consist of a 1.5 m refractive coronagraph that will observe the corona from $1.03 R_{sun}$ to $2.0 R_{sun}$ with a 2 arcsec spatial resolution and will provide magnetic field measurements with a 10 minute cadence down to a 1 G sensitivity. The instrument will also be allowed to have an offset observation mode that will extend its field of view up to $4.0 R_{sun}$ above the limb to follow the evolution of CMEs at large distances. A more complete description of the COSMO suite can be found in the COSMO website (<http://www2.hao.ucar.edu/cosmo>).

The UCoMP project serves as a pathfinder for the larger LC instrument. Once operational, UCoMP will enable the determination of the intensity levels for the lines in Table 1 for COSMO LC instrument design. Further, it will provide a testbed to experiment on other lines not included in Table 1 which could provide valuable diagnostics for the solar corona, the solar wind and CME plasmas. With its vastly larger aperture, COSMO will dramatically improve the diagnostic capabilities over UCoMP at all heights, especially for magnetic field measurements. Also, the COSMO project includes a planned joint

HAO/University of Michigan data analysis and modeling facility which will provide the necessary infrastructure to fully distribute and utilize COSMO data for space weather modeling and forecasting, and for student involvement in cutting edge scientific research.

6. Summary

Visible observations of the solar corona provide a wealth of opportunities to address the open problems in solar physics, such as coronal heating, solar wind acceleration, and CME triggering and evolution to name a few. Visible coronagraphs can be (and have been) deployed on the ground and in space; however, their diagnostic potential has not been fully exploited yet, especially because of lack of observations of individual spectral lines for sufficiently large fields of view, even though eclipse observations have fully demonstrated their potential. In this paper we have reviewed the diagnostic techniques that can be applied to visible observations of spectral line intensities, and some of the open problems in solar physics that they can help us address. The upcoming ground-based visible coronagraphs – UCoMP, under development, and COSMO, under study – will provide unprecedented opportunities to expand our understanding of our star, of its evolution, and of its effects on the heliosphere and our own planet.

Acknowledgments. EL and ST acknowledge support from NSF grant AGS-1408789; EL and SRH also acknowledge support from NSF grant AGS-1255704. The National Center for Atmospheric Research is sponsored by the National Science Foundation. This is a review paper about plasma diagnostic techniques, and does not contain any data.

References

Arnaud, J., & Newkirk G. Jr. 1987, A&A, 178, 263

- Bak-Steslicka, U., Gibson, S.E., Fan, Y., Bethge, C., Forland, B., & Rachmeler, L.A. 2013, ApJ, 770, L28
- Cram, L.E. 1976, Sol. Phys. 48, 3
- Cranmer, S.R., van Ballegoijen, A.A., & Edgar, R.J. 2007, ApJS, 171, 520
- Del Zanna, G., Dere, K.P., Young, P.R., Landi, E., & Mason, H.E. 2015, A&A, 582, 56
- Frazin, R.A., Lamy, P., Llebaria, A., & Vasquez, A.M. 2010, ApJ, 715, 1352
- Habbal, S.R., Morgan, H., Johnson, J., Arndt, M.B., Daw, A., Jaeggli, S., Kuhn, J., & Mickey, D. 2007, ApJ, 663, 598
- Habbal, S.R., Druckmüller, M., Morgan, H. et al., 2010a, ApJ, 708, 1650
- Habbal, S.R., Druckmüller, M., Morgan, H. et al., 2010b, ApJ, 719, 1362
- Habbal, S.R., Morgan, H., Druckmüller, M., & Ding, A. 2010c, ApJL, 711, L75
- Habbal, S.R., Druckmüller, M., Morgan, H. et al., 2011, ApJ, 734, 120
- Habbal, S.R., Morgan, H., & Druckmüller, M. 2014, ApJ, 739, 119
- Hahn, M., Landi, E., & Savin, D.W. 2012, ApJ, 753, 36
- Hayes, A.P., Vourlidas, A., & Howard, R.A. 2001, ApJ, 548, 1081
- Judge, P.G., Casini, R., Tomczyk, S., Edwards, D.P., & Francis, E. 2001, *Coronal Magnetometry: a feasibility study*, NCAR/HAO technical report NCAR/TN-446+STR
- Judge, P.G., Habbal, S.R., & Landi, E. 2013, Sol. Phys., 288, 467
- Landi, E. 2008, ApJ, 685, 1270
- Landi, E., & Bhatia, A.K. 2012, ADNDT, 89, 862
- Landi, E., Gruesbeck, J.R., Lepri, S.T., & Zurbuchen, T.H. 2012a, ApJ, 750, 159
- Landi, E., Alexander, R.L., Gruesbeck, J.R., Gilbert, J.A., Lepri, S.T., Manchester, W.B., & Zurbuchen, T.H. 2012b, ApJ, 744, 100

Figure 1. Composite image of the eclipse observation of 2010 July 11 (white light, in blue) with the corresponding SDO/AIA 171 Å taken at the same time (yellow) (courtesy of Karen Teramura). The individual large scale plasma structures seen in the inner corona by SDO seamlessly blend with those observed in the outer corona from during the eclipse.

- Landi, E., Oran, R., Lepri, S.T., Zurbuchen, T.H., Fisk, L.A., van der Holst, B. 2014, ApJ, 790, 111
- Lin, H., Kuhn, J.R., & Coulter, R. 2004, ApJL, 613, L177
- Lyot, B. 1932, Zeitschrift für Astrophysik, 5, 73
- McCracken, K.G., Beer, J., Steinhilber, F., & Abreu, J. 2013, Sp. Sci. Rev., 176, 89
- Phillips, K.J.H., Feldman, U., & Landi, E. 2008, *Ultraviolet and X-ray Spectroscopy of the Solar Atmosphere*, Cambridge Astrophysics Series 44, Cambridge University Press, Cambridge, UK
- Rachmeler, L.A., Gibson, S.E., Dove, J.B., DeVore, C.R., & Fan, Y. 2013, Sol. Phys, 288, 6170
- Skomorovski, V.I., Trifonov, V.D., Mashnich, G.P., Zagaynova, Y.S., Fainshtein, V.G., Kushtal, G.I., & Chuprakov, S.A. 2012, Sol. Phys., 277, 267
- Smartt, R.N., Dunn, R.B., and Fisher, R.R. 1981, Proc. SPIE, 288, 395
- Tian, H., Tomczyk, S., McIntosh, S.W., Bethge, C., de Toma, G., & Gibson, S.E. 2013, Sol. Phys., 288, 637
- Tomczyk, S., McIntosh, S.W., Keil, S.L., Judge, P.G., Schad, T., Seeley, D.H., & Edmondson, J. 2007, Science, 317, 1192
- Tomczyk, S., Card, G.L., Darnell, T., Elmore, D.F., Lull, R., Nelson, P.G., Ständer, K.V., Burkepile, J., Casini, R., & Judge, P. 2008, Solar Physics, 247, 411
- Tomczyk, S., Casini, R., de Wijn, A.G. and Nelson, P.G. 2010, Ap. Opt., Vol. 49, No. 18., 3580-3586
- van de Hulst, H.C., 1950, Bull. Astr. Inst. Neth., 11, 135
- van der Holst, B., Sokolov, I.V., Meng, X., et al. 2014, ApJ, 782, 81

Figure 2. **Top:** Sections of the corona as observed in Fe XI during the 2006 eclipse. **Middle panels:** Intensities of spectral line emission as a function of radial distance given as solid lines, with the color coding corresponding to the traces in the top panels. Continuum intensities are shown as dashed curves. **Bottom panels:** Corresponding ratio of line to continuum intensities. The regions where collisional excitation and resonance excitation dominate are indicated. Also shown for the example on the right is the freezing-in distance where the ratio of line to continuum becomes flat. The presence of localized enhancement in the ratio appears in the left panel. [See Habbal et al. 2007]

Figure 3. Overlay of Fe X 6374 Å (red) and Fe XI 7892 Å (cyan) [left], and Fe X 6374 Å (red) and Fe XIV 5303 Å (green) emission [right] from the 2010 eclipse observations. [From Habbal et al. 2011]

Figure 4. Example of comparison between predicted and observed line intensities, for the Na IX 681.72 Å observed by SOHO/SUMER in an off-disk coronal hole (Landi 2008). Blue full line intensities were predicted using the MIC code, dashed lines were predicted using ionization equilibrium at the local temperatures. The full and dashed green lines mark the limb and the maximum height reached by spicules (which invalidate the comparison), respectively. **Left panel:** Cranmer et al. (2007) coronal hole/fast wind model. **Right panel:** Empirical model with the wind source region located in the corona (from Landi et al. 2014).

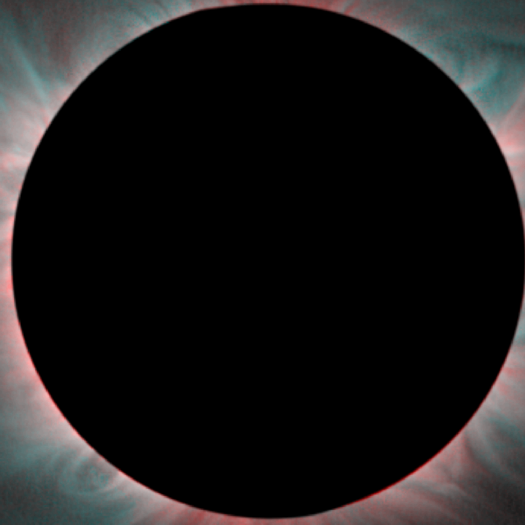
Figure 5 **Left:** Current field of view of CoMP (blue region): the images at the wavelength of the emission line and of the continuum are formed on the same 1024×1024 pixel detector. **Right:** UCoMP field of view (blue region): the two wavelengths will be imaged onto two different detectors, each 1280×1024 pixel, resulting in a much larger field of view.

CME core		CME hot component		Quiescent corona	
Line	$\log T_{eff}$	Line	$\log T_{eff}$	Line	$\log T_{eff}$
H I 6564	4.01-4.29	Fe XIV 5303	6.15-6.49	Fe X 6374	5.80-6.24
He I 5887	4.01-4.57	Fe XV 7062	6.20-6.63	Fe XI 7894	5.92-6.30
He I 10833	4.01-4.57	S XII 7613	6.16-6.55	Fe XIII 10800 (Ne)	6.08-6.41
Ca II 8544	4.01-4.34	Ar XIII 8339 (Ne)	6.26-6.67	Fe XIII 10749 (Ne)	6.08-6.41
O II 7321	4.16-4.92	Ar XIII 10143 (Ne)	6.26-6.67	Fe XIV 5303	6.15-6.49
O II 7332	4.16-4.92	Ca XV 5446 (Ne)	6.44-6.84	Ar X 5535	5.86-6.42
O III 5008	4.62-5.23	Ca XV 5695 (Ne)	6.44-6.84	Ar XI 6918	6.04-6.52
Fe VI 5177	4.95-5.52				

Table 1. Visible lines that will be observed by UCoMP. Wavelengths are in Å. Lines from the same ion indicated with “Ne” provide density sensitive line pairs. $\log T_{eff}$ indicates the temperature range where each ion has fractional abundance 0.01 or larger under equilibrium conditions.

ot

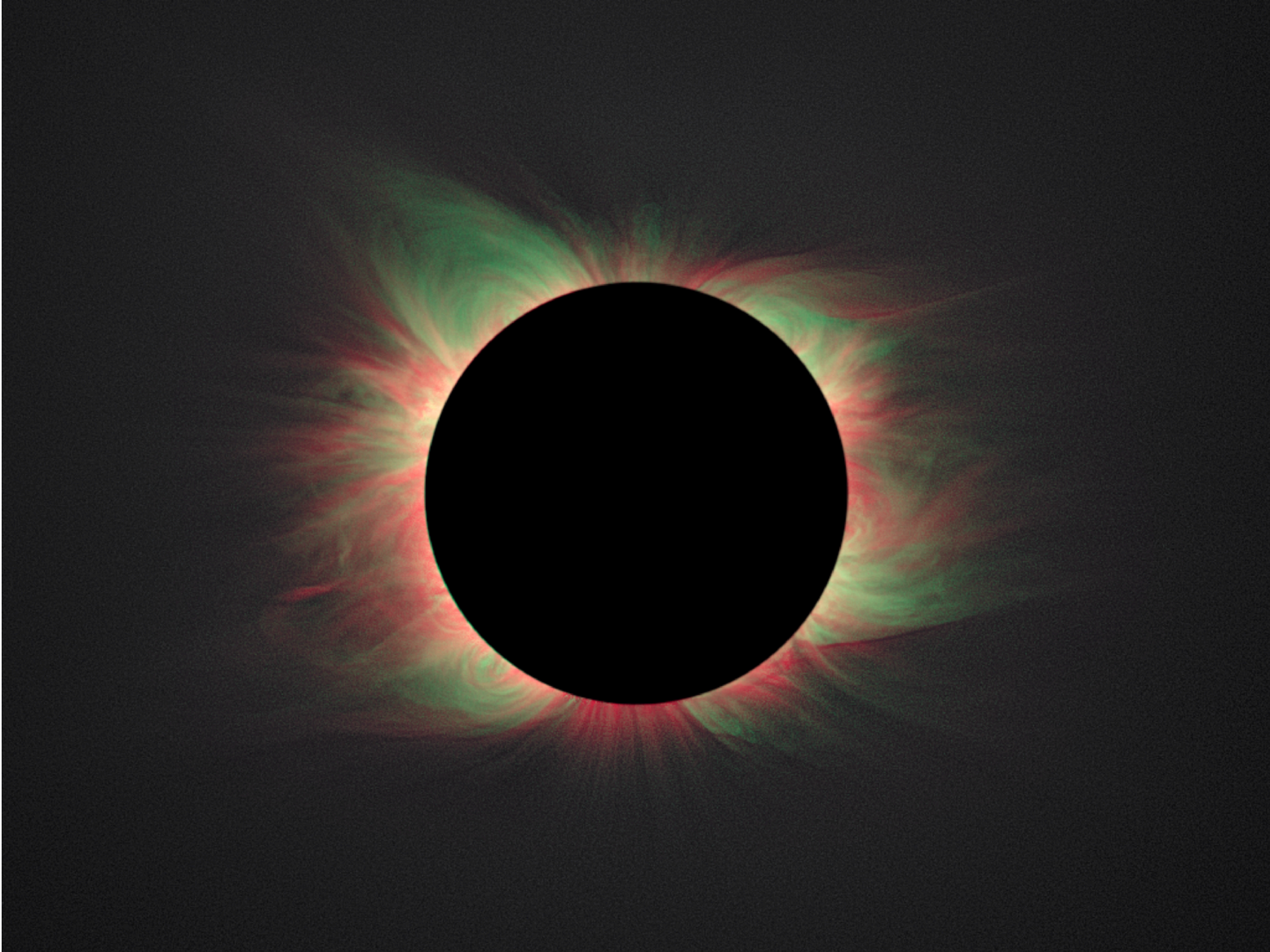
A



2016ja022598-f01-z-.eps

ot

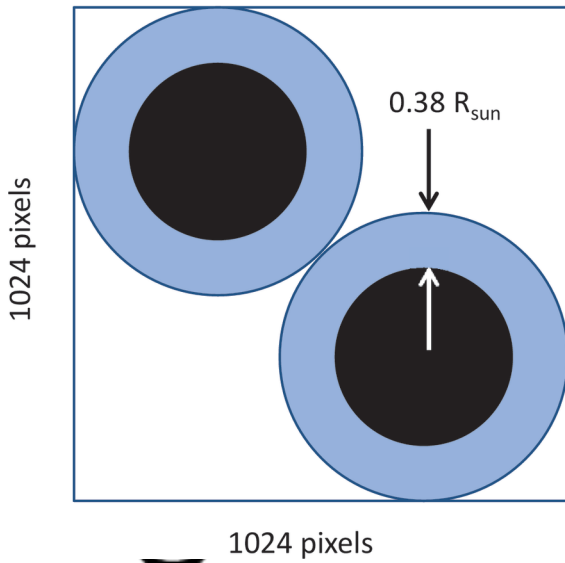
A



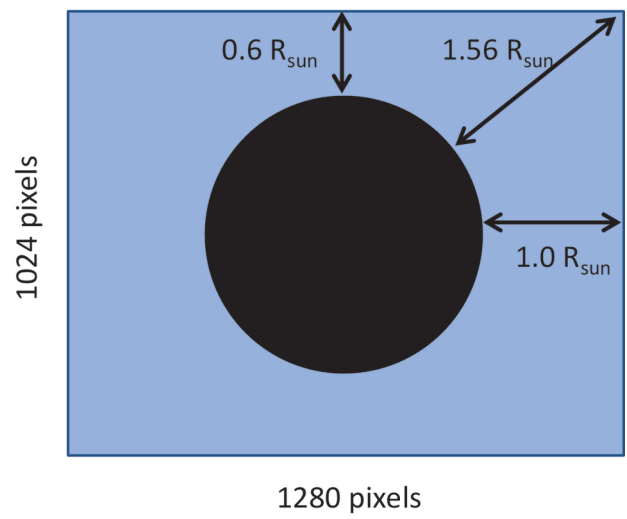
2016ja022598-f02-z-.eps

script

CoMP Field-of-View



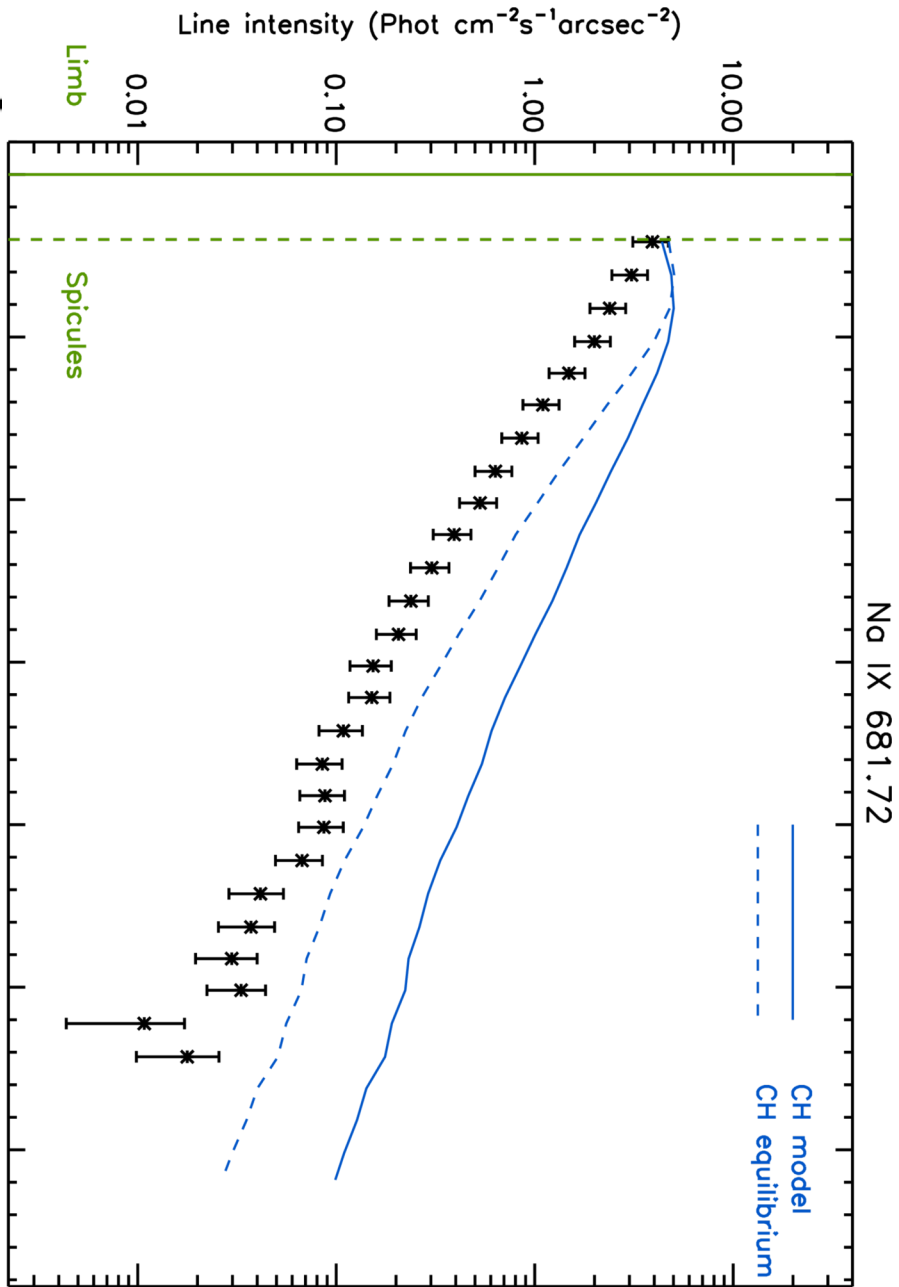
UCoMP Field-of-View



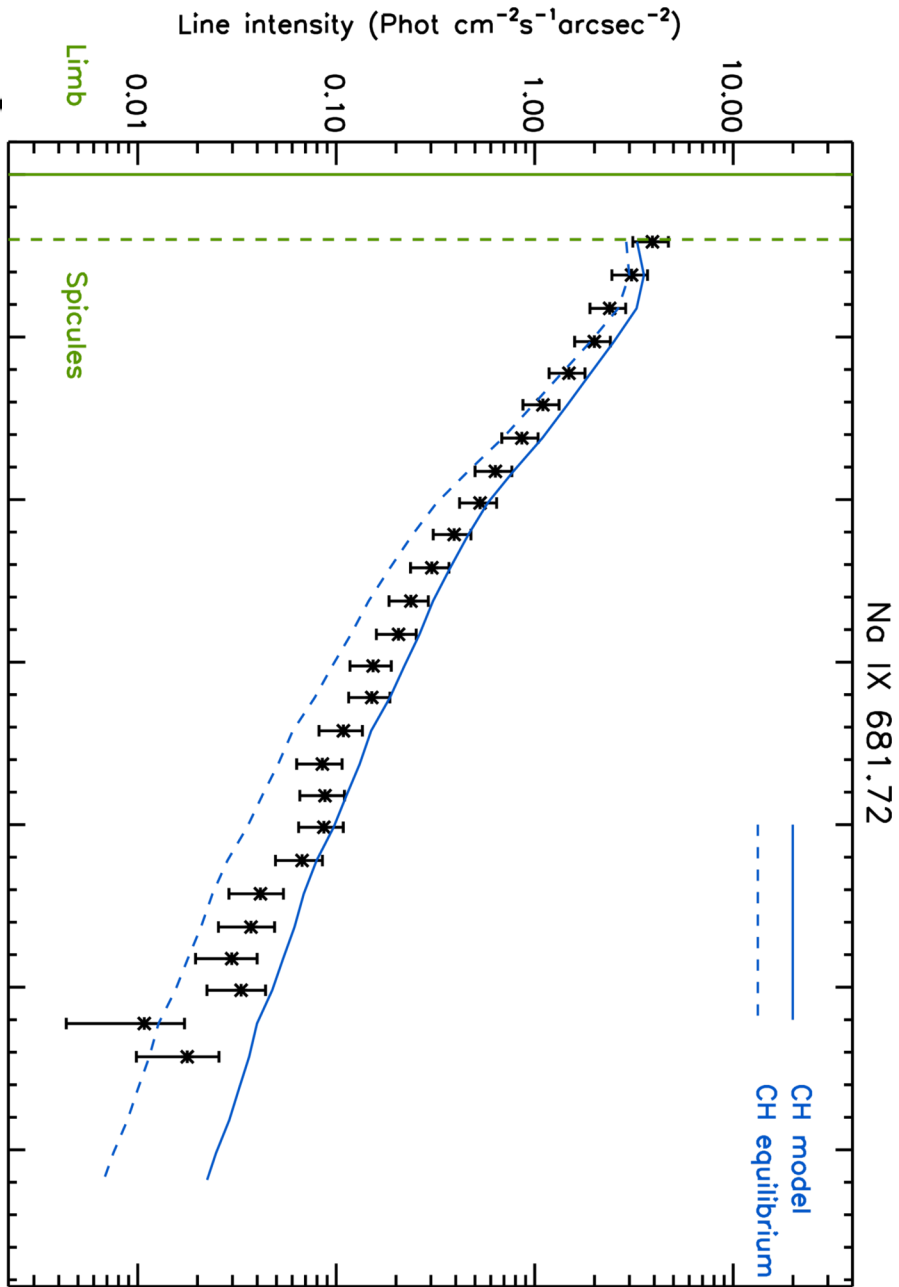
Auth

1024 pixels

2016ja022598-f03-z-eps

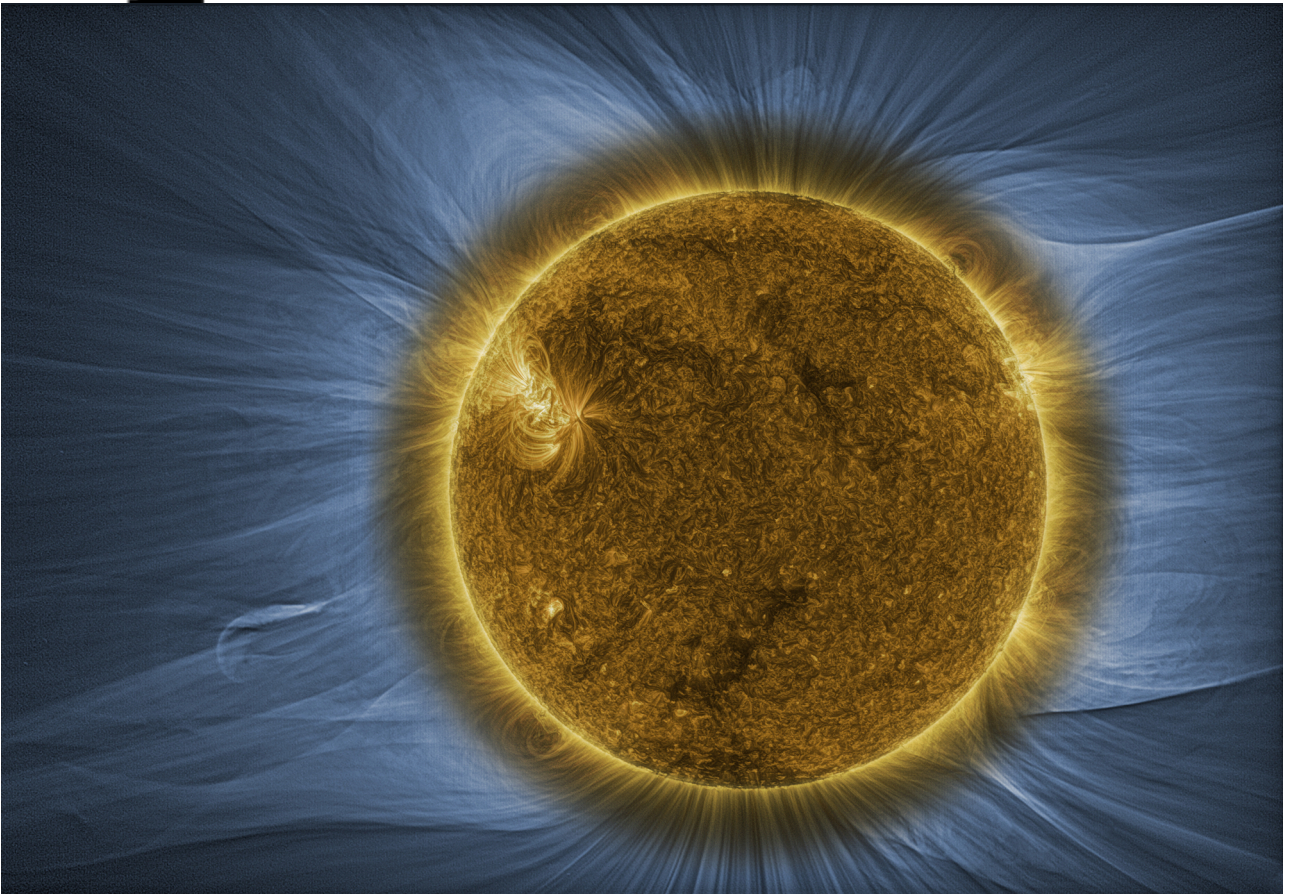


2016ja022598-f04-z-.eps



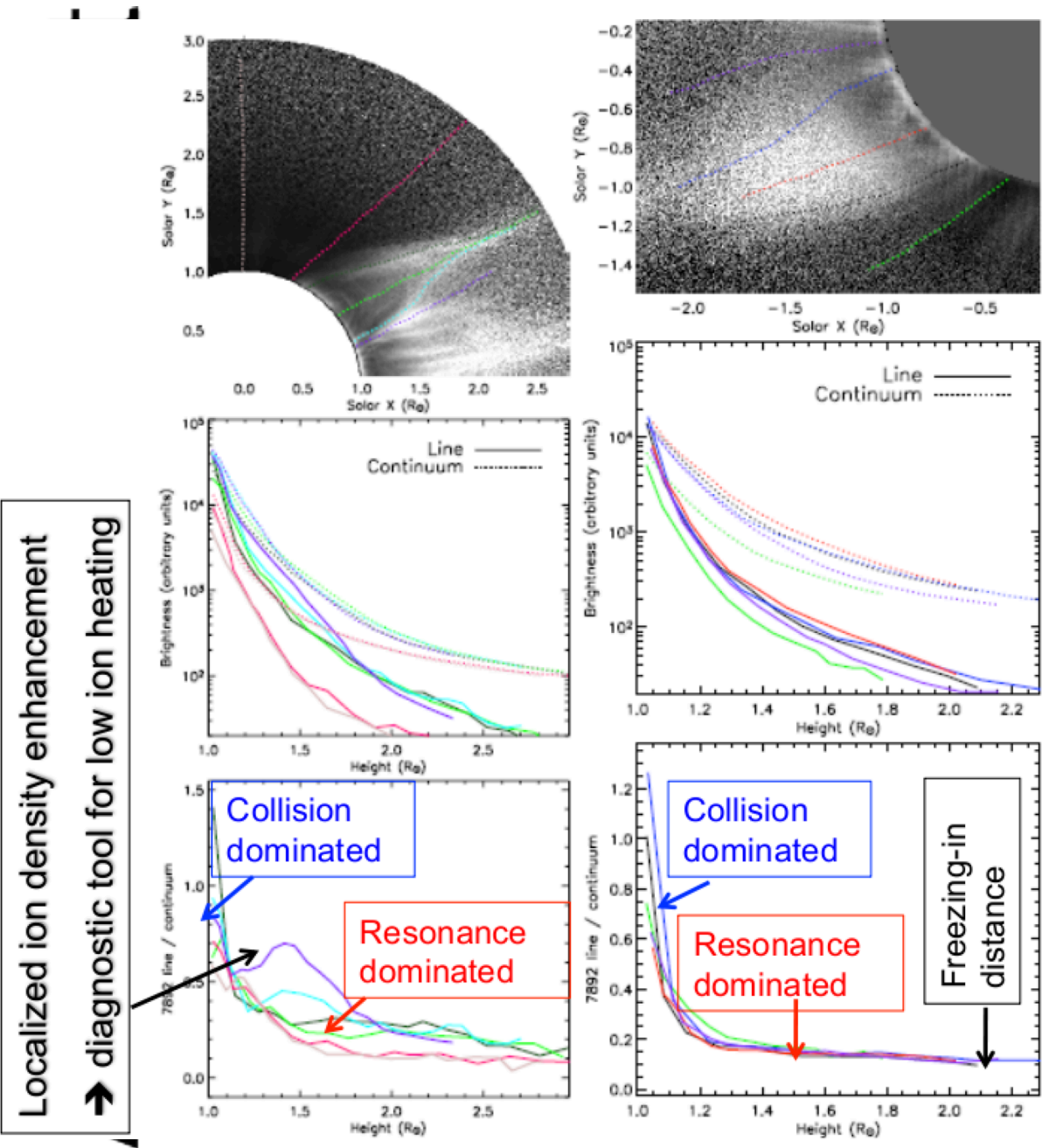
2016ja022598-f05-z-.eps

ript



2016ja022598-f06-z-.eps

Au-



2016ja022598-f07-z-.eps